ARTICLE

https://doi.org/10.1038/s41586-018-0365-y

Coherent spin–photon coupling using a resonant exchange qubit

A. J. Landig[1,4]*, J. V. Koski[1,4], P. Scarlino[1], U. C. Mendes[2], A. Blais[2,3], C. Reichl[1], W. Wegscheider[1], A. Wallraff[1], K. Ensslin[1] & T. Ihn[1]

Electron spins hold great promise for quantum computation because of their long coherence times. Long-distance coherent coupling of spins is a crucial step towards quantum information processing with spin qubits. One approach to realizing interactions between distant spin qubits is to use photons as carriers of quantum information. Here we demonstrate strong coupling between single microwave photons in a niobium titanium nitride high-impedance resonator and a three-electron spin qubit (also known as a resonant exchange qubit) in a gallium arsenide device consisting of three quantum dots. We observe the vacuum Rabi mode splitting of the resonance of the resonator, which is a signature of strong coupling; specifically, we observe a coherent coupling strength of about 31 megahertz and a qubit decoherence rate of about 20 megahertz. We can tune the decoherence electrostatically to obtain a minimal decoherence rate of around 10 megahertz for a coupling strength of around 23 megahertz. We directly measure the dependence of the qubit–photon coupling strength on the tunable electric dipole moment of the qubit using the 'AC Stark' effect. Our demonstration of strong qubit–photon coupling for a three-electron spin qubit is an important step towards coherent long-distance coupling of spin qubits.

The ability to transmit quantum information over long distances is desirable for quantum information processors[1]. Circuit quantum electrodynamics provides a well-established platform for connecting distant qubits[2]: microwave photons in a superconducting waveguide resonator couple to the electric dipole moment of multiple qubits, which are fabricated close to the resonator. Strong qubit–photon coupling has been realized with superconducting qubits[3] and, recently, the coherence properties of charge qubits in semiconductor quantum dots have improved sufficiently to enable strong coupling[4–6]. Even better coherence is expected by transferring the quantum information from electron charge to spin[7,8]. However, this approach comes with a major challenge because the coupling of photons to spins is several orders of magnitude weaker than their coupling to charge[9]. This challenge can be overcome by introducing an electric dipole moment to the spin states. For single-electron spin qubits, spin and charge are coupled by using materials with strong spin–orbit coupling[10], devices with ferromagnetic leads[11] or a magnetic-field gradient generated by an on-chip micromagnet[12–14]. A different approach is realized in the resonant exchange qubit[15–19], in which the spin exchange interaction couples two states with an equal three-electron charge distribution and equal total spin, but different spin arrangements. This interaction also gives rise to an electrical dipole moment that enables coherent qubit–photon coupling. Here, we implement such a three-electron spin qubit in a circuit quantum electrodynamics architecture[20,21] hosted in GaAs and achieve strong spin–photon coupling, as evident from the observation of vacuum Rabi mode splitting. Both the spin decoherence and the qubit–photon coupling strength can be controlled electrostatically[22].

Quantum device

In Fig. 1a, b we show optical and scanning electron micrographs of our hybrid quantum device. Electrons are trapped in a triple-quantum-dot structure by electrostatic confinement created by gold gates (Fig. 1b) on top of a GaAs/AlGaAs heterostructure. The heterostructure hosts a two-dimensional electron gas 90 nm below the surface of the triple-quantum-dot region, which has a mobility of $\mu = 3.2 \times 10^6$ cm^2 V^{-1} s^{-1} and an electron density of $n_e = 2.2 \times 10^{11}$ cm^{-2} at 4.2 K. The electrostatic potentials of the left, middle and right quantum dots are tuned using the respective plunger-gate voltages V_L, V_M and V_R. A quantum point contact acts as a charge sensor that allows us to determine the charge configuration of the triple quantum dot. We operate the triple quantum dot as a three-electron spin qubit[19], as discussed in detail below.

To couple the qubit to microwave photons, the plunger gate of the left quantum dot extends to the superconducting microwave resonator (Fig. 1a). The left plunger gate is also DC-biased via a resistive gold line, which is connected to the field anti-node of the centre conductor of the resonator. The coupling strength g_s between qubit and resonator photons is proportional to the square root of the characteristic impedance of the resonator ($\sqrt{Z_r}$)[6,23]. It is enhanced by fabricating the resonator, as shown in Fig. 1a, from a thin (about 15 nm) and narrow (roughly 300 nm) centre conductor made of the high-kinetic-inductance material NbTiN[24]. We estimate $Z_r = \sqrt{L_l/C_l} \approx 1.3\,\mathrm{k\Omega}$, with $L_l \approx 150\,\mu\mathrm{H\,m^{-1}}$ ($C_l \approx 90\,\mathrm{pF\,m^{-1}}$) the inductance (capacitance) of the resonator per unit length, which results in an enhancement in the coupling strength by a factor of five compared to a standard impedance-matched $Z_r = 50\,\Omega$ resonator. Our choice of material and design allows us to operate the resonator in the presence of an external magnetic field applied parallel to the plane of the resonator[24]. In the experiments described here, we apply a magnetic field of $B_{ext} = 200$ mT.

Strong spin–qubit–photon coupling

To demonstrate strong coupling of the spin qubit with a microwave photon, we first detune the transition frequency of the qubit from the resonance frequency of the resonator. In this detuned situation, we determine a resonator resonance frequency of $\nu_r = 4.38$ GHz and a line width of $\kappa/(2\pi) = 47.1$ MHz at an average photon occupation of less than 1 (see inset of Fig. 1c). When the spin qubit is tuned into resonance with the resonator, we observe two distinct peaks in the

[1]Department of Physics, ETH Zürich, Zurich, Switzerland. [2]Institut quantique and Département de Physique, Université de Sherbrooke, Sherbrooke, Quebec, Canada. [3]Canadian Institute for Advanced Research, Toronto, Ontario, Canada. [4]These authors contributed equally: A. J. Landig, J. V. Koski. *e-mail: alandig@phys.ethz.ch

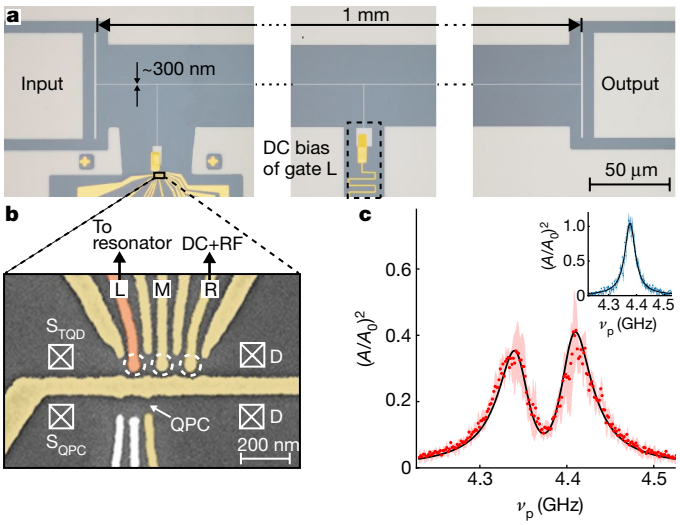

Fig. 1 | Hybrid quantum device and vacuum Rabi splitting. a, Optical micrograph of the device split into three parts, showing the resonator, which is capacitively coupled to the input and output transmission lines. The region for the DC bias of gate L (see **b**) that connects to the centre of the resonator is indicated as a dashed black rectangle. **b**, False-colour scanning electron micrograph of the gate structure defined by electron beam lithography. The two white gates are kept at zero voltage in our experiments. The gate highlighted in orange is electrically connected to the resonator. The approximate positions of the left, middle and right quantum dots are indicated by dashed white circles; their corresponding plunger gates are labelled 'L', 'M' and 'R'. The right plunger gate is biased with both DC and microwave (RF) signals. The triple quantum dot and quantum point contact (QPC) have separate ohmic source contacts (S_{TQD} and S_{QPC}) and a common drain contact (D). **c**, Resonator transmission $(A/A_0)^2$ as a function of resonator probe frequency ν_p for the uncoupled (blue, inset) and coupled (red, main plot) configuration, showing vacuum Rabi mode splitting as a result of strong spin–photon coupling. The standard deviation of repeated measurements is indicated by the shaded region. The qubit parameters for the coupled configuration are specified in Fig. 4. The solid black lines are fits to an input–output model[25].

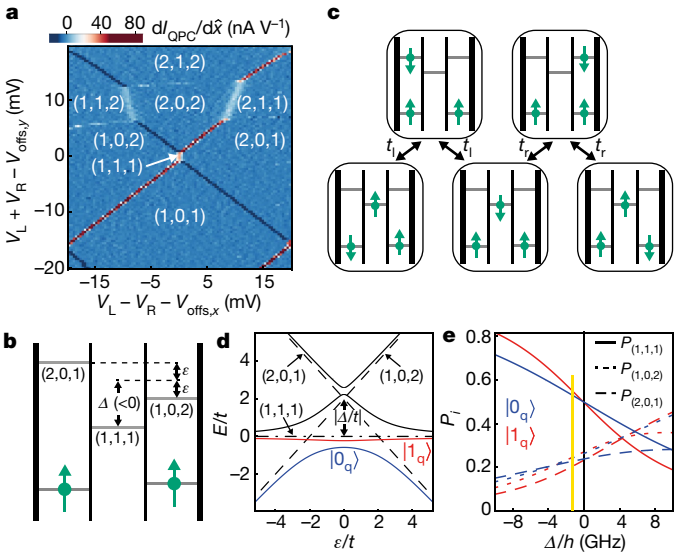

Fig. 2 | Spin-qubit operation regime. a, Differential quantum point contact current $dI_{QPC}/d\hat{x}$, where $\hat{x} = V_L - V_R - V_{offs,x}$, as a function of different combinations of plunger gate voltages V_L and V_R. $V_{offs,x}$ and $V_{offs,y}$ are voltage offsets in the x and y directions. **b**, Schematic of the triple quantum dot, defining the asymmetry and detuning parameters ε and Δ, respectively. The three grey lines indicate the possible energy levels for the addition of the third electron. **c**, Illustration of the three electron states in the triple quantum dot that form the spin qubit. The states mix via tunnel couplings t_l and t_r. **d**, Eigenenergies E/t of the system illustrated in **c** as a function of ε/t for $\Delta/t = -2$ and symmetric tunnel coupling $t_l = t_r = t$. Dashed lines indicate the energy of the charge states (2, 0, 1) and (1, 0, 2) for $t_l = t_r = 0$. The dash-dotted line is the eigenenergy of the $S = 3/2$, $S_z = 1/2$ state, which does not couple to any of the other states (Supplementary Information, section S1). This line also corresponds to the energy of the (1, 1, 1) states for $t_l = t_r = 0$. The spin-qubit states $|0_q\rangle$ (blue) and $|1_q\rangle$ (red) are highlighted. **e** Probabilities $P_{(1,1,1)}$ (solid lines), $P_{(2,0,1)}$ (dashed lines) and $P_{(1,0,2)}$ (dotted lines), as defined in the main text, for $|0_q\rangle$ (blue) and $|1_q\rangle$ (red) as a function of Δ/h. The plot is obtained for $t_l/h = 9.04$ GHz, $t_r/h = 7.99$ GHz and $\varepsilon/h = -1.03$ GHz. The position in Δ/h at which Fig. 1c was recorded is indicated by the yellow line.

transmission spectrum (Fig. 1c). This splitting of the resonance of the resonator into two well-separated peaks, known as vacuum Rabi mode splitting, is the characteristic signature of strong coherent hybridization of a single microwave photon in the resonator and the spin qubit in the triple quantum dot. From a fit of the vacuum Rabi splitting to an input–output model[25], we extract a qubit–photon coupling strength of $g_s/(2\pi) = 31.4 \pm 0.3$ MHz and a qubit decoherence rate of $\gamma_2/(2\pi) = 19.6 \pm 0.5$ MHz. These values confirm that our quantum device operates in the strong coupling regime, which is supported by the fact that the approximate peak separation is larger than the widths of peaks, $2g_s > \kappa/2 + \gamma_2$. This is our main result; we provide more details on how it was achieved below.

Triple-quantum-dot spin qubit

The spin qubit is formed by tuning the triple quantum dot into the three-electron regime. In Fig. 2a we show the charge stability diagram of the triple quantum dot, as measured by the charge detector. Regions with different charge configurations (k, l, m) are indicated, where the integers k, l and m express the number of electrons in the three dots. The qubit operation point is located in the narrow (1, 1, 1) region between the (2, 0, 1) and (1, 0, 2) regions. As illustrated in Fig. 2b, we introduce an asymmetry parameter ε and a detuning parameter Δ to quantify differences in the energies $E(i)$ of the three relevant charge configurations i in the absence of interdot tunnelling: $\varepsilon = [E(2,0,1) - E(1,0,2)]/2$ and $\Delta = E(1,1,1) - [E(2,0,1) + E(1,0,2)]/2$. Both parameters are tuned experimentally using the plunger-gate voltages: ε increases by increasing V_L and decreasing V_R, whereas Δ increases by increasing V_L and V_R while decreasing V_M. Other charge configurations are not relevant, because the charging energies of the quantum dots are of the order of 1 meV (240 GHz), much larger than the thermal energy $k_B T = 3\,\mu$eV (620 MHz) for our experiments, which were performed at an electronic temperature of $T = 30$ mK (and where k_B is the Boltzmann constant).

In general, there are eight different spin configurations for three spins. For the asymmetric charge configurations (2, 0, 1) and (1, 0, 2), the three triplet states within the doubly occupied dots do not play a part because the singlet–triplet splitting of roughly 1 meV (240 GHz) is much larger than the temperature[7]. This leaves us with two relevant spin configurations for each of the two asymmetric charge configurations. Two of them, each with a z component of total spin of $S_z = 1/2$, are depicted in the top row of Fig. 2c. The other two are obtained by flipping the spin in the singly occupied dot, giving $S_z = -1/2$. These spin configurations of the asymmetric charge configurations couple by tunnelling to the spin configurations of the (1, 1, 1) charge configuration. The qubit states are formed by a coherent superposition of the five basis states with $S_z = 1/2$ (Fig. 2c)[19]. An equivalent set of basis states with $S_z = -1/2$, which differs only in the Zeeman energy, exists but is not depicted. Mixing of these different S_z states by an Overhauser field of about 5 mT[7] is suppressed by the much larger externally applied magnetic field. The (1, 1, 1) states couple via the exchange interaction between electrons in neighbouring dots: an electron in the middle dot can be exchanged with an electron of opposite spin in the left or right dot by tunnelling to the asymmetric charge state.

We do not consider the (1, 1, 1) state with $S_z = 3/2$ because, for our choice of external magnetic field ($B_{ext} = 200$ mT), its energy is more

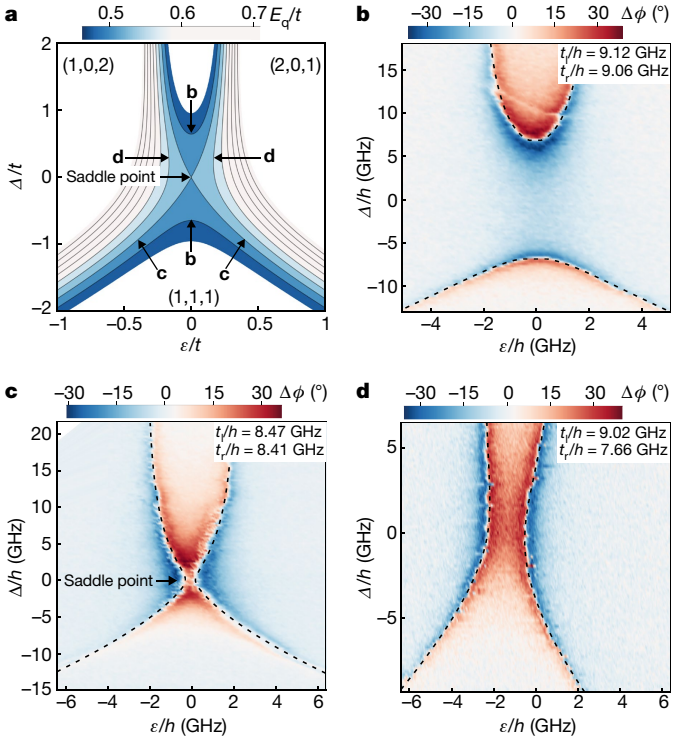

Fig. 3 | Resonator response. a, Contour plot of the normalized qubit energy E_q/t for symmetric tunnel coupling t as a function of the asymmetry and detuning parameters ε/t and Δ/t. The energy contours probed in **b**–**d** are labelled, as is the saddle point in the qubit energy. The energetically favoured three-electron charge configurations are also indicated. **b**–**d**, Phase difference $\Delta\phi$ of the signal transmitted through the resonator, measured on-resonance for different tunnel-coupling configurations t_l and t_r. The dashed lines indicate fits to the theoretical qubit energy contours (see **a**).

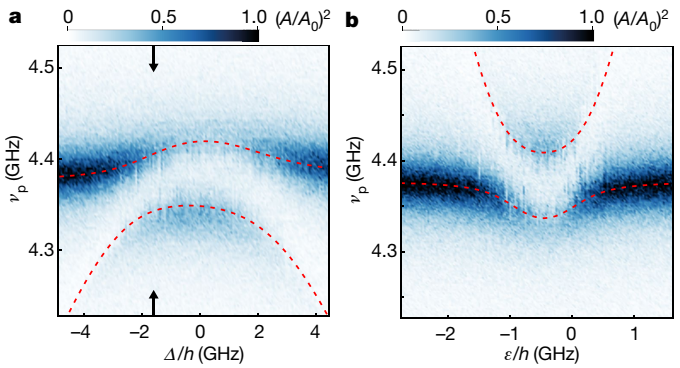

Fig. 4 | Resonator spectrum at the saddle point in the qubit energy. **a**, Resonator transmission $(A/A_0)^2$ as a function of probe frequency ν_p and detuning Δ for $\varepsilon/h = -1.03$ GHz, $t_l/h = 9.04$ GHz and $t_r/h = 7.99$ GHz. The arrows indicate the position of the vacuum Rabi mode splitting shown in Fig. 1c. **b**, Resonator transmission as a function of asymmetry ε for $\Delta/h = 0.23$ GHz, $t_l/h = 8.25$ GHz and $t_r/h = 8.64$ GHz. The dashed lines in **a** and **b** are the eigenenergies of the coupled qubit–resonator system.

than $h \times 1$ GHz higher than the excited-state energy of the qubit (where h is the Planck constant). It therefore does not form the ground state of the system and does not coherently couple via fluctuations in the Overhauser field to the qubit states. The $S_z = 3/2$ state becomes relevant for $B_{ext} \geq 1$ T (see Supplementary Information, section S3).

The two lowest-energy eigenstates of the system define the ground $|0_q\rangle$ and the excited $|1_q\rangle$ state of the qubit, which has energy $E_q(\Delta, \varepsilon, t_l, t_r) = E_{|1_q\rangle} - E_{|0_q\rangle}$, where $t_{l(r)}$ is the tunnel coupling between the middle dot and the left (right) dot (see Fig. 2d). In the limit $\Delta \ll -t_{l,r}$, the qubit states predominantly have the same charge configuration—(1, 1, 1)—and are given by $|0_q\rangle \approx |0\rangle \equiv (|\uparrow,\uparrow,\downarrow\rangle - |\downarrow,\uparrow,\uparrow\rangle)/\sqrt{2}$ and $|1_q\rangle \approx |1\rangle \equiv (2|\uparrow,\downarrow,\uparrow\rangle - |\uparrow,\uparrow,\downarrow\rangle - |\downarrow,\uparrow,\uparrow\rangle)/\sqrt{6}$ (ref. 19; Supplementary Information, section S1). Because both qubit states have the same total spin of 1/2, the finite qubit energy is not determined by an external magnetic field but by the exchange interaction (which is proportional to t^2/Δ) between the $|0\rangle$ and $|1\rangle$ spin states, thus realizing the resonant exchange qubit. In this regime, the qubit is minimally influenced by charge noise, but also couples weakly to photons. In the other extreme ($\Delta \gg t_{l,r}$), the qubit states are dominated by different charge configurations—(2, 0, 1) and (1, 0, 2)—and are therefore of charge character (see Fig. 2e). Such a charge qubit has a strong electric dipole moment and is susceptible to charge noise, but also couples more strongly to resonator photons. We operate our qubit in the regime $|\Delta| \lesssim t_{l,r}$, in which we quantify the spin and charge character of the qubit states as follows: for each of the qubit states $|0_q\rangle$ and $|1_q\rangle$, we define $P_{(1,1,1)}$ to be the sum of the occupation probabilities of the three (1, 1, 1) basis states, and $P_{(2,0,1)}$ and $P_{(1,0,2)}$ to be the occupation probabilities of the (2, 0, 1) and (1, 0, 2) states, respectively. These quantities depend on Δ, as depicted in Fig. 2e, in which t_l, t_r and ε are the same as for the measurement of the vacuum Rabi mode splitting in Fig. 1c.

The value of $\Delta/h = -1.44$ GHz used for the vacuum Rabi measurement is indicated in Fig. 2e by a vertical yellow line, at which point both qubit states have a high $P_{(1,1,1)}$. A majority of the quantum information is stored in the spin degree of freedom, providing protection from charge decoherence. On the other hand, a finite qubit–photon coupling is generated by the admixture with asymmetric charge states[20,21], apparent as finite $P_{(1,0,2)}$ and $P_{(2,0,1)}$ in Fig. 2e, similarly to other spin–qubit implementations[26,27]. The amount of charge admixture and hence the nature of the qubit in our system is electrostatically tunable with the parameter Δ. This is quantified in the spin–photon coupling strength g_s, which is approximated in our qubit-operation regime as $g_s = [1/2 + \sqrt{2}/24 \times (3 + \sqrt{3})\Delta/t]g_c$, where g_c is the charge–photon coupling strength (Supplementary Information, section S2). We obtain $g_c/(2\pi) = 71$ MHz from the vacuum Rabi measurement in Fig. 1c.

Qubit–resonator interaction

Next we probe the energy spectrum of the qubit with the resonator. The theoretically expected lines of constant qubit energy as a function of detuning Δ and asymmetry ε are indicated in Fig. 3a. At constant and equal tunnel couplings, the qubit energy exhibits a saddle point at $\varepsilon = \Delta = 0$, (labelled in Fig. 3a). At this point, the qubit energy is insensitive to dephasing in the ε and Δ directions to first order[22]. To extract contours of qubit energy, we apply a microwave probe tone at frequency ν_p on-resonance with the resonator ($\nu_p = \nu_r$), tune the qubit energy E_q with ε and Δ, and measure the phase of the signal that is transmitted through the resonator (Fig. 3b–d). We observe a phase shift whenever the qubit and the resonator approach a resonance, $E_q = h\nu_r$. When the resonance is crossed, the phase changes sign. Determining these transition points in the ε–Δ plane experimentally at fixed tunnel couplings maps the energy contour $E_q(\Delta, \varepsilon) = h\nu_r$, reproducing one of the theoretically expected energy contours shown in Fig. 3a. We map different energy contours by changing the tunnel coupling. This is realized experimentally by changing the electrical potential of the gate lines between the plunger gates (see Fig. 1b).

From Fig. 3b to Fig. 3d, we increase the average tunnel coupling to map different contour lines of E_q (as labelled in Fig. 3a). We obtain the magnitude of both tunnel barriers for Fig. 3b–d from a fit to the resonance positions of the phase-response data. A simultaneous fit to the three datasets in Fig. 3b–d reduces the number of free parameters (Supplementary Information, section S4) and results in excellent agreement between theoretical and measured resonance conditions. The tunability of the position of the resonator–qubit resonance via the tunnel coupling allows us to observe qubit–photon coupling at the saddle point in the qubit energy in Fig. 3c. Note that, as observed in

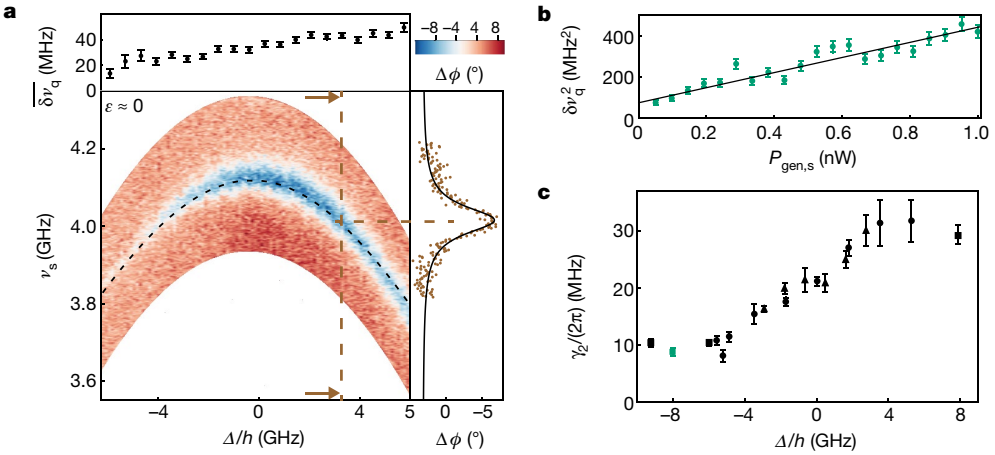

Fig. 5 | Qubit spectroscopy. a, Phase response of the resonator probed on-resonance as a function of spectroscopy frequency ν_s and detuning Δ, with ε set to the minimum of the qubit energy in ε ($\varepsilon \approx 0$), for $t_l/h = 8.10$ GHz, $t_r/h = 7.86$ GHz, a drive-generator power of $P_{gen,s} = 0.75$ nW and a resonator photon occupation of less than 1. The theoretically expected position of the phase-response minimum is indicated by a dashed line. On the right, a Lorentzian with a half-width at half-maximum of $\delta\nu_q$ (black line) is fitted to a cut of the phase response (brown dashed line in the main panel; brown points). At the top we show $\overline{\delta\nu_q}$ (points), which is the average of $\delta\nu_q$ over five subsequent cuts along Δ, along with its standard error (error bars). **b**, Dependence of $\delta\nu_q^2$ (with standard errors) on the drive-generator power $P_{gen,s}$, measured at $\Delta/h = -8.03$ GHz and with ε set to the minimum of the qubit energy in ε, for $t_l/h = 8.74$ GHz and $t_r/h = 8.12$ GHz. The solid line is a fit to the expected linear dependence. **c**, Extracted qubit decoherence $\gamma_2/(2\pi)$ (with standard errors) as a function of Δ for three different tunnel-coupling configurations: $t_l/h = 8.74$ GHz and $t_r/h = 8.12$ GHz (squares), $t_l/h = 7.47$ GHz and $t_r/h = 7.77$ GHz (triangles), and $t_l/h = 8.10$ GHz and $t_r/h = 7.86$ GHz (circles). The value obtained from the linear fit in **b** is shown in green.

Fig. 3d, this point is shifted and the energy contours are tilted for asymmetric barriers[19].

To characterize the strength of the resonator–qubit interaction further, we tune the qubit to a similar tunnel coupling configuration as in Fig. 3c, such that qubit and resonator are resonant at the saddle point in the qubit energy. We measure the resonator transmission spectra as a function of Δ with ε set to the minimum of the qubit energy in ε (Fig. 4a), and as a function of ε with Δ set to the maximum of the qubit energy in Δ (Fig. 4b). Both transmission spectra show a clear anti-crossing of qubit and resonator over a large range of detuning Δ and asymmetry ε. This anti-crossing is due to the strong coherent hybridization of the spin qubit and single microwave photons in the resonator. The eigenenergies of the coupled system are obtained via numerical diagonalization of the Jaynes–Cummings Hamiltonian. They agree with the experimentally observed transmission maxima in Fig. 4a, b.

The transmission spectra also confirm the saddle point in the qubit energy: in Fig. 4a we observe an energy maximum of the qubit around $\Delta \approx 0$; in Fig. 4b the qubit energy has a minimum around $\varepsilon \approx 0$. Note that the vacuum Rabi splitting shown in Fig. 1c and discussed above is obtained for $\varepsilon/h = -1.03$ GHz and $\Delta/h = -1.44$ GHz, as indicated by the two arrows in Fig. 4a.

Tunable qubit coherence and coupling strength

To characterize the spin qubit further, we now consider the shift in the resonator frequency due to qubit–resonator coupling in the dispersive regime, in which the qubit–resonator detuning is much larger than the qubit–photon coupling strength[28]. In addition to the resonator probe tone at frequency $\nu_p = \nu_r$, a spectroscopy tone at frequency ν_s is applied to the right plunger gate, indicated in Fig. 1b. At resonance with the qubit ($E_q = h\nu_s$), the drive excites the qubit from its ground state $|0_q\rangle$ to the excited state $|1_q\rangle$. This results in a dispersive shift in the resonator frequency, which we detect as a drop in the phase-response signal. By sweeping both the detuning Δ and the spectroscopy frequency ν_s, with ε set to the minimum of the qubit energy in ε, we trace the spectroscopic qubit signal (Fig. 5a). This signal resembles the Δ dependence of the observed (Fig. 4a) and calculated (Fig. 3a) qubit energy and is in good agreement with theory (dashed line in Fig. 5a).

The qubit decoherence $\gamma_2/(2\pi)$ is equal to the half-width at half-maximum ($\delta\nu_q$) of the spectroscopic dip in the phase signal in the limit of zero drive power ($P_{gen,s} \to 0$)[28]. For finite drive power, such as in Fig. 5a, the spectroscopic signal is power-broadened[28]. We define $\overline{\delta\nu_q}$ as the average of $\delta\nu_q$ over five cuts along the Δ direction in Fig. 5a and observe an increase in $\overline{\delta\nu_q}$ with increasing Δ (top panel of Fig. 5a). To distinguish the effects of power broadening and qubit decoherence on $\delta\nu_q$, we extract γ_2 (Fig. 5c) by measuring $\delta\nu_q$ as a function of the power of the spectroscopy tone (Fig. 5b) for different Δ and three different tunnel-coupling configurations. We estimate the Purcell decay and the measurement-induced dephasing to be at least one order of magnitude smaller than $\gamma_2/(2\pi)$ (Fig. 5c)[28,29]. For a high admixture of asymmetric charge states, we measure a maximum decoherence rate of $\gamma_2/(2\pi) \approx 30$ MHz. For a spin qubit with a more (1, 1, 1)-like character, we extract a minimum decoherence rate of $\gamma_2/(2\pi) \approx 10$ MHz, which corresponds to a dephasing time of $T_2^* = 1/\gamma_2 = 16$ ns. This measurement demonstrates that storing the quantum information in the spin degree of freedom increases the coherence of the qubit.

For a theoretical model that describes the data in Fig. 5c quantitatively, different sources of noise would need to be considered[30]. Charge noise that originates from electric-field fluctuations such as gate-voltage noise leads to dephasing, which is minimal at the saddle point in the qubit energy. We observe that γ_2 is not minimal at this point ($\Delta \approx 0$ in Fig. 5c). This indicates that other noise sources, such as second-order charge-noise dephasing or phonons, are responsible for the observed qubit decoherence[31]. Another source of noise is the fluctuating Overhauser field in the GaAs host material[32], which leads to inhomogeneous broadening of the line width of the qubit. This is a likely explanation for the lower limit of $\gamma_2/(2\pi) \approx 10$ MHz in Fig. 5a, consistent with previous studies that reported similar dephasing times for a resonant exchange qubit[33] and other spin qubits in GaAs[34,35]. To distinguish and quantify the contributions of the aforementioned noise sources to the experimental qubit decoherence, additional analysis such as time-resolved measurements is necessary.

Finally, we show that the average photon number in the resonator is well below 1 for the measurement of the Rabi splitting. In the dispersive regime, the qubit frequency ν_q shifts as a function of the number of photons n in the resonator, which depends linearly on the power $P_{gen,r}$ at the generator of the resonator probe tone. In addition, there is a Lamb shift in the qubit frequency due to the coupling to vacuum fluctuations. This results in a dressed qubit frequency $\tilde{\nu}_q = \nu_q + (2n+1)[g_s/(2\pi)]^2/(\nu_q - \nu_r)$ (ref. 28). In Fig. 6a, we observe

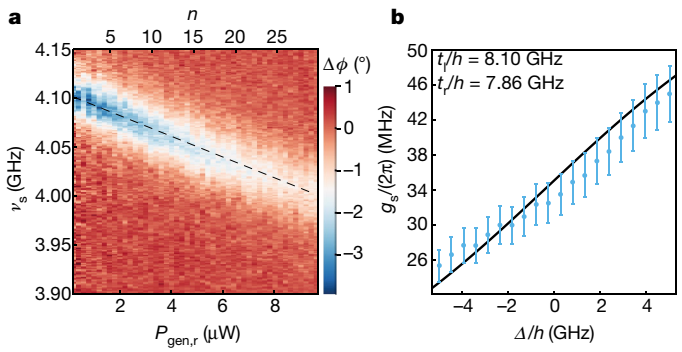

Fig. 6 | AC Stark shift. a, Phase response as a function of spectroscopy frequency ν_s and the power $P_{gen,r}$ at the generator of the resonator probe tone. $P_{gen,r}$ is converted to the average number of photons in the resonator n. The drive-generator power is set to $P_{gen,s} = 0.25$ nW and the resonator is probed on-resonance. The qubit parameters are tunnel couplings $t_l/h = 8.72$ GHz and $t_r/h = 8.18$ GHz, detuning $\Delta/h = -6.0$ GHz and asymmetry $\varepsilon/h = -0.26$ GHz. The minimum in the phase response is indicated by a dashed line. **b**, Spin-qubit–photon coupling strength g_s, with errors from the calibration of the photon number, as a function of Δ (points), compared to the prediction from theory (line) for ε close to the minimum of the qubit energy in ε.

the frequency shift due to the AC Stark shift in the spectroscopic qubit signal measured at $\Delta/h = -6.02$ GHz and $\varepsilon/h = -0.26$ GHz. At this operating point, we obtain g_s from an independent measurement of the shift in the resonator frequency, similar to the one displayed in Fig. 4b (Supplementary Information, section S5). From a linear fit to the power-dependent dressed qubit frequency in Fig. 6a, we obtain the calibration factor $\alpha = n/P_{gen,r} \approx 3 \times 10^{-3}$ photons nW^{-1}. The vacuum Rabi splitting shown in Fig. 1c was recorded for $P_{gen,r} = 100$ nW. We can therefore reliably claim that for this measurement the average number of photons in the resonator is roughly 0.3. This confirms that we indeed achieved strong hybridization of the spin qubit with a single microwave photon.

With the known calibration factor α, the AC Stark shift provides direct access to the qubit–photon coupling strength (Supplementary Information, section S5). We observe in Fig. 6b that the coupling strength increases with increasing Δ. Because the contribution of the (1, 0, 2) and (2, 0, 1) charge configurations to the qubit states increases with Δ, the electric dipole moment of the qubit states and hence the qubit–resonator coupling is enhanced. However, this increase in coupling strength comes at the cost of an increase in qubit decoherence (see Fig. 5c). Our theoretical model describes this behaviour quantitatively.

Conclusion

We have coherently coupled a resonant exchange qubit to single microwave photons in a circuit quantum electrodynamics architecture. The triple-quantum-dot spin qubit arises from the exchange interaction, which couples spin and charge independent of the host material. Other spin-qubit implementations have been restricted to materials with strong spin–orbit coupling[10] or require additional components such as ferromagnets[11,26,27] for spin–charge hybridization. Furthermore, the triple-quantum-dot spin qubit is versatile because all of its parameters can be controlled electrostatically. For these reasons, it is possible to move our architecture to material systems with minimal hyperfine interaction, such as graphene[36] or isotopically purified silicon[8], without the need to deposit ferromagnetic materials, which is generally undesirable in the presence of a superconductor. By doing so, we expect the qubit coherence to improve by at least one order of magnitude.

While writing up our results we became aware of independent but related work that demonstrates strong spin–photon coupling in a double-quantum-dot spin qubit in silicon[26,27].

Data availability

The data related to this study are available from the corresponding author on reasonable request.

Received: 4 January 2018; Accepted: 19 June 2018;
Published online: 25 July 2018

1. DiVincenzo, D. P. The physical implementation of quantum computation. *Fortschr. Phys.* **48**, 771–783 (2000).
2. Majer, J. et al. Coupling superconducting qubits via a cavity bus. *Nature* **449**, 443–447 (2007).
3. Wallraff, A. et al. Strong coupling of a single photon to a superconducting qubit using circuit quantum electrodynamics. *Nature* **431**, 162–167 (2004).
4. Bruhat, L. E. et al. Strong coupling between an electron in a quantum dot circuit and a photon in a cavity. Preprint at https://arxiv.org/abs/1612.05214 (2016).
5. Mi, X., Cady, J. V., Zajac, D. M., Deelman, P. W. & Petta, J. R. Strong coupling of a single electron in silicon to a microwave photon. *Science* **355**, 156–158 (2017).
6. Stockklauser, A. et al. Strong coupling cavity QED with gate-defined double quantum dots enabled by a high impedance resonator. *Phys. Rev. X* **7**, 011030 (2017).
7. Hanson, R., Kouwenhoven, L. P., Petta, J. R., Tarucha, S. & Vandersypen, L. M. K. Spins in few-electron quantum dots. *Rev. Mod. Phys.* **79**, 1217–1265 (2007).
8. Zwanenburg, F. A. et al. Silicon quantum electronics. *Rev. Mod. Phys.* **85**, 961–1019 (2013).
9. Schoelkopf, R. J. & Girvin, S. M. Wiring up quantum systems. *Nature* **451**, 664–669 (2008).
10. Petersson, K. D. et al. Circuit quantum electrodynamics with a spin qubit. *Nature* **490**, 380–383 (2012).
11. Viennot, J. J., Dartiailh, M. C., Cottet, A. & Kontos, T. Coherent coupling of a single spin to microwave cavity photons. *Science* **349**, 408–411 (2015).
12. Pioro-Ladrière, M. et al. Electrically driven single-electron spin resonance in a slanting Zeeman field. *Nat. Phys.* **4**, 776–779 (2008).
13. Hu, X., Liu, Y.-x. & Nori, F. Strong coupling of a spin qubit to a superconducting stripline cavity. *Phys. Rev. B* **86**, 035314 (2012).
14. Beaudoin, F., Lachance-Quirion, D., Coish, W. A. & Pioro-Ladrière, M. Coupling a single electron spin to a microwave resonator: controlling transverse and longitudinal couplings. *Nanotechnology* **27**, 464003 (2016).
15. Medford, J. et al. Quantum-dot-based resonant exchange qubit. *Phys. Rev. Lett.* **111**, 050501 (2013).
16. Medford, J. et al. Self-consistent measurement and state tomography of an exchange-only spin qubit. *Nat. Nanotechnol.* **8**, 654–659 (2013).
17. Gaudreau, L. et al. Coherent control of three-spin states in a triple quantum dot. *Nat. Phys.* **8**, 54–58 (2012).
18. Taylor, J. M., Srinivasa, V. & Medford, J. Electrically protected resonant exchange qubits in triple quantum dots. *Phys. Rev. Lett.* **111**, 050502 (2013).
19. Russ, M. & Burkard, G. Asymmetric resonant exchange qubit under the influence of electrical noise. *Phys. Rev. B* **91**, 235411 (2015).
20. Srinivasa, V., Taylor, J. M. & Tahan, C. Entangling distant resonant exchange qubits via circuit quantum electrodynamics. *Phys. Rev. B* **94**, 205421 (2016).
21. Russ, M. & Burkard, G. Long distance coupling of resonant exchange qubits. *Phys. Rev. B* **92**, 205412 (2015).
22. Russ, M., Ginzel, F. & Burkard, G. Coupling of three-spin qubits to their electric environment. *Phys. Rev. B* **94**, 165411 (2016).
23. Devoret, M., Girvin, S. & Schoelkopf, R. Circuit-QED: how strong can the coupling between a Josephson junction atom and a transmission line resonator be? *Ann. Phys.* **16**, 767–779 (2007).
24. Samkharadze, N. et al. High-kinetic-inductance superconducting nanowire resonators for circuit QED in a magnetic field. *Phys. Rev. Appl.* **5**, 044004 (2016).
25. Collett, M. J. & Gardiner, C. W. Squeezing of intracavity and traveling-wave light fields produced in parametric amplification. *Phys. Rev. A* **30**, 1386–1391 (1984).
26. Mi, X. et al. A coherent spin–photon interface in silicon. *Nature* **555**, 599–603 (2018).
27. Samkharadze, N. et al. Strong spin-photon coupling in silicon. *Science* **359**, 1123–1127 (2018).
28. Schuster, D. I. et al. ac Stark shift and dephasing of a superconducting qubit strongly coupled to a cavity field. *Phys. Rev. Lett.* **94**, 123602 (2005).
29. Sete, E. A., Gambetta, J. M. & Korotkov, A. N. Purcell effect with microwave drive: suppression of qubit relaxation rate. *Phys. Rev. B* **89**, 104516 (2014).
30. Russ, M. & Burkard, G. Three-electron spin qubits. *J. Phys. Condens. Matter* **29**, 393001 (2017).
31. Mehl, S. & DiVincenzo, D. P. Noise analysis of qubits implemented in triple quantum dot systems in a Davies master equation approach. *Phys. Rev. B* **87**, 195309 (2013).
32. Hung, J.-T., Fei, J., Friesen, M. & Hu, X. Decoherence of an exchange qubit by hyperfine interaction. *Phys. Rev. B* **90**, 045308 (2014).
33. Malinowski, F. K. et al. Symmetric operation of the resonant exchange qubit. *Phys. Rev. B* **96**, 045443 (2017).
34. Petta, J. R. Coherent manipulation of coupled electron spins in semiconductor quantum dots. *Science* **309**, 2180–2184 (2005).
35. Koppens, F. H. L., Nowack, K. C. & Vandersypen, L. M. K. Spin echo of a single electron spin in a quantum dot. *Phys. Rev. Lett.* **100**, 236802 (2008).
36. Trauzettel, B., Bulaev, D. V., Loss, D. & Burkard, G. Spin qubits in graphene quantum dots. *Nat. Phys.* **3**, 192–196 (2007).

Acknowledgements We acknowledge discussions with M. Russ and A. Stockklauser. We thank M. Collodo, P. Kurpiers and P. Märki for contributions to our experimental set-up. This work was supported by the Swiss National Science Foundation through the National Center of Competence in Research (NCCR) Quantum Science and Technology. U.C.M. and A.B. were supported by NSERC and the Canada First Research Excellence fund.

Reviewer information *Nature* thanks T. Meunier and the other anonymous reviewer(s) for their contribution to the peer review of this work.

Author contributions A.J.L., J.V.K. and P.S. fabricated the device. A.J.L. and J.V.K. performed the experiments. A.J.L. and J.V.K. analysed the data. U.C.M. and A.B. provided theory support for the experiment. C.R. and W.W. grew the wafer material. A.J.L., J.V.K., T.I. and U.C.M. wrote the manuscript with the input of all authors. A.W., K.E. and T.I. supervised the experiment.

Competing interests The authors declare no competing interests.

Additional information

Supplementary information is available for this paper at https://doi.org/10.1038/s41586-018-0365-y.

Correspondence and requests for materials should be addressed to A.J.L.